Journal of Electroanalytical Chemistry 1013 (2026) 120104

Contents lists available at ScienceDirect

Journal of Electroanalytical Chemistry

journal homepage: www.elsevier.com/locate/jeac

Investigation of CR-39 damaging mechanisms in electrochemical environments

Kimmo Pyyhtiä [a,*], Jerzy J. Jasielec [a], Tom Sillanpää [b], Jere Hyvönen [b], Rainer Götz [c], Lilian Moumaneix [d], Vincent Martin [e], Arnaud Viola [e], Frédéric Maillard [e], Tanja Kallio [d], Ari Salmi [b], Elena Gubanova [c], Aliaksandr Bandarenka [c,f], Pekka Peljo [a,d,*]

[a] Department of Mechanical and Materials Engineering, University of Turku, Vesilinnantie 5, 20500 Turku, Finland
[b] Electronics Research Laboratory, Department of Physics, University of Helsinki, Helsinki, Finland
[c] Physics of Energy Conversion and Storage, TUM School of Natural Sciences, Department of Physics, Technical University of Munich, James-Franck-Str. 1, 85748 Garching, Germany
[d] Department of Chemistry and Materials Science, School of Chemical Engineering, Aalto University, Kemistintie 1, 02150 Espoo, Finland
[e] LEPMI, Université Grenoble Alpes, Université Savoie-Mont-Blanc, CNRS, Grenoble-INP, 38000 Grenoble, France
[f] Catalysis Research Center TUM, Ernst-Otto-Fischer-Str. 1, 85748 Garching bei München, Germany

ARTICLE INFO

Keywords:
CR-39
Co-deposition
Oxyhydrogen
Recombination
Cavitation

ABSTRACT

Poly(allyl diglycol carbonate), CR-39, is a common type of plastic used in detecting and measuring radiation exposure. Incident particles damage the polymer, leaving behind latent tracks. During chemical etching, these tracks are then preferentially etched, resulting in microscale tracks where the particles have passed. In electrochemical cells, pits in CR-39 detectors have been used as evidence for presence of nuclear reactions during palladium–deuterium co-deposition. This research focuses on replicating these measurements and investigating parameters affecting pit formation. With appropriate cell designs, pits can be produced without palladium and/or deuterium in the system. Free radical formation and cavitation are proposed as alternative CR-39 damaging mechanisms. CR-39 response to ultrasound cavitation indicates cavitation as the predominant source of the initial damage on CR-39 surfaces. Pits produced during metal-hydride/deuteride co-deposition and subsequent hydrogen evolution reaction (HER) processes after etching had their diameters distributed into two partially overlapping normal distributions. Comparisons with literature suggested this diametral distribution bifurcation could be the result of cavitation collapse of two types of evolved gas nanobubbles. Spherical nanobubbles and high contact angle surface nanobubbles produce jets during their collapse, creating seed damages relative to their projection, with the spherical bubble collapse producing deeper impressions. Surface damage differences on CR-39 surface are then magnified during the etching process resulting in the observed diametral distributions. The results of this study indicate that work involving CR-39 detectors in systems with gas evolution should take cavitation effects into account, as polymer-damaging cavitation events occur during electrolysis. They also underline that CR-39 detectors can serve as a tool to characterize degradation caused by cavitation in electrolyzers.

1. Introduction

Poly(allyl diglycol carbonate), also known as CR-39, is a solid state nuclear track detector (SSNTD) widely employed due to its chemical stability, versatility in detecting multiple different types of radiation, and its ability to record radiation exposure in low flux condition [1]. CR-39 operates on the principle that an energetic particle entering the detector bulk breaks polymer chains along its flight path leaving behind a track of damaged polymer chains known as a latent track. When the detector material is etched with a corrosive solution, such as concentrated NaOH, the material is etched preferentially along the latent track leaving behind a microscale track. CR-39 detectors can be used to detect alpha particles [2], protons [3], neutron radiation [4,5] and even X-rays [6], with proper pretreatments required for the latter two. Interestingly, radiation-like features (referred to as pits when describing generic surface damage in this work) have been reported also when palladium metal is electrodeposited in the presence of evolving deuterium gas to achieve high deuterium loading ratios, in process termed as Pd-D co-deposition [7–11], suggesting the presence of low

* Corresponding authors.
E-mail addresses: kitapy@utu.fi (K. Pyyhtiä), pekka.peljo@utu.fi (P. Peljo).

https://doi.org/10.1016/j.jelechem.2026.120104
Received 14 November 2025; Received in revised form 31 March 2026; Accepted 3 April 2026
Available online 17 April 2026

energy nuclear reactions. Pd-D co-deposition can also be considered as electrodeposition at such potentials where D_2 evolution and insertion into the Pd lattice takes place. Recently, Chen et al. [12] have shown that electrochemical loading of Pd lattices with deuterium increases probability of nuclear fusion events when the metal is bombarded with deuterium ions in vacuum, showing that there are interesting effects when loading Pd with D. Energetic particles impacting organic polymers are known to induce free radical formation, molecular emission, double bond formation and chain scission [13,14]. CR-39 radiation exposure has been linked to increased presence of CO_2, and OH-group signals in infrared absorption spectra, suggesting that C–O–C and C = O bond breakage lead to the initial localized damage being amplified due released CO_2 gas leaving behind lower density regions and by the increased local OH-group concentration, thus promoting etching along the latent track [15]. Free radicals are created during water electrolysis through the formation of H_2O_2 and its subsequent decomposition into hydroxyl ($^{\bullet}OH$) and hydroperoxyl ($HOO^{\bullet}$) radicals. In polymer exchange membrane water electrolyzers, hydrogen peroxide can be formed when oxygen diffuses through the membrane to the anode and is reduced [16,17]. OH-group radicals are known to be a considerable factor in degradation of proton-exchange membrane fuel cells [18–20].

In addition to radical induced damage, recombination of oxygen and hydrogen gasses generated during water electrolysis has been suggested to create explosive shock waves with capacity to damage CR-39 surfaces [21]. Hydrogen and oxygen nanobubbles grown on Ti thin films with alternating potentials have been reported to merge together and to spontaneously explode via surface-assisted combustion mechanism, with the resulting steam vapor cloud expanding into micrometer dimensions before rapidly collapsing due to the external liquid pressure [22,23]. Collapse of the vapor cloud was also associated with formation of secondary cavitation bubbles that upon collapsing exert forces greater than the metal electrode shear strength and thus stripping nanoparticles from the electrode surface. Alternatively, surface or free spherical nanobubbles can collapse directly via a shock-induced mechanism without the need for explosive recombination [24]. Cavitation is mainly pressure-driven phenomenon where the internal pressure of a gas-filled bubble is overcome by pressure exerted by the surrounding medium, resulting in the violent collapse of the bubble. Cavitation collapse of nano- and microscale bubbles is characterized by formation of microjets that impact nearby liquid–solid interfaces with the damage profile being dependent on the bubble size and distance from the surface [24–26].

In this work, we have reproduced Pd-H/D co-deposition experiments, and with the preliminary results indicating that pits could be produced in both H_2O and D_2O with appropriate cell geometry, we continued to explore alternative explanations in free radical formation and cavitation for the observed CR-39 damage. Possible nuclear transmutations were excluded with inductively coupled plasma mass spectrometry (ICP-MS). Comparisons of the etched pits produced in co-deposition and cavitation experiments suggested similar origins and these were related to computational works on cavitation collapses and by simulating the CR-39 etching process.

2. Experimental

Experimental measurements in this work were divided into three main experimental sets. (i) Palladium-electrodeposition (PdE) measurements focused on replication and further examination of Pd-H/D co-deposition. (ii) Recombination cell (RCC) experiments investigated the recombination of oxygen and hydrogen gasses and radical damage. (iii) Polymer cavitation damage (PCD) measurements examined the damage caused by cavitation damage induced by high-intensity focused ultrasound (HIFU).

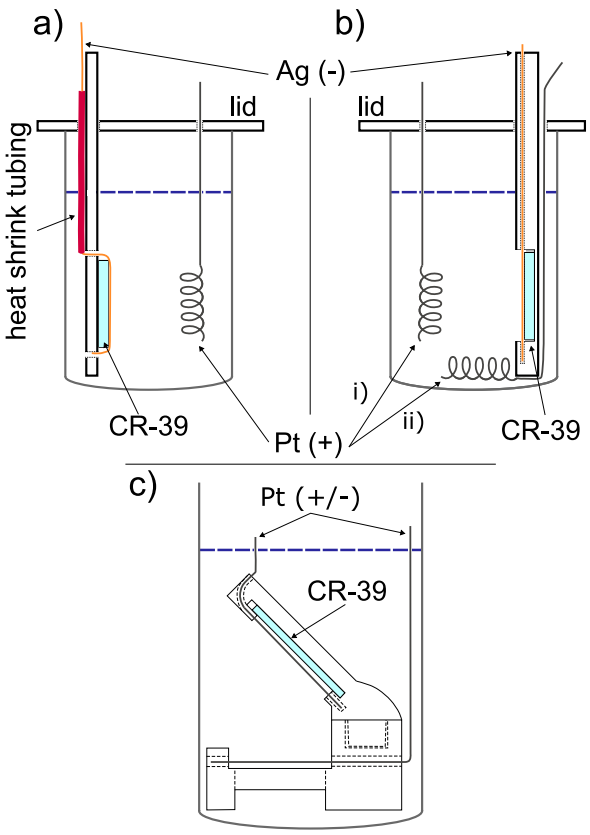

Fig. 1. (a) Schematic of the cell type where CR-39 was tied with fishing line (not pictured). (b) Updated 3D-printed cell design enabled better application of protective films. Pt counter electrode was used first opposite the WE (i), later being placed underneath it (ii). (c) 3D-printed cells used in RCC-experiments had the CR-39 pieces at an angle.

2.1. Palladium electrodeposition

Metal-hydride co-deposition was studied with the cell displayed in Fig. 1a. The cells were constructed by placing a 0.25 mm diameter Ag wire (Sigma-Aldrich 99,99%) working electrode (WE) on top of CR-39 (TechnoTrak 2, Chiyoda Technol) pieces (cut to ca. 10 mm by 20 mm), and tied to a polycarbonate support using monofilament fishing line. Detector orientation was marked on top right corners of the detector fronts with an arrow. On the back side of the support the Ag wire was covered with polyolefin heat shrinking tubing. In later experiments, the support was substituted with a 3D-printed cell (3DC) holders printed from PLA (Prusament) were used to simplify the cell construction and to enable the use of protective films between the Ag wire and CR-39 piece, as illustrated in Fig. 1b. Counter electrode (CE) of choice was a coiled 0.5 mm Pt wire (Jalometallitukku Bergman 99,9%) with surface area of approximately 1.6 cm^2. Platinum was excluded in a few experiments with the use of a dimensionally stabilized anode (DSA) composed of titanium mesh with RuO_2 and IrO_2 coatings (>9 g/m^2 Ru + Ir, GuangYi Store, China) with 8.5 cm^2 surface area. All electrodes were submerged in 10% nitric acid (VWR) solution for a minute and rinsed before cell assembly. It should be noted that the purities of the working electrodes used are relatively low, possibly introducing small concentrations contaminants, such Ag or Au, into the electrolytes. H-cell experiments were performed using a cell with two 30 mL chambers separated by a Nafion-117 (IonPower) cationic exchange membrane.

Solutions/electrolytes were prepared by dissolving $PdCl_2$ (Sigma-Aldrich 99,9%), $CuCl_2$ (Sigma-Aldrich 99.995%), $PdNO_3$ hydrate (Sigma-Aldrich, ≤ 100%) or $PtCl_2$ (Sigma-Aldrich 99.99%) in either ultrapure

Table 1
Different experiments and their electrolyte compositions used in the PdE measurements. For twin experiments, the parameters are identical unless otherwise noted with boldface font, most commonly indicating D_2O as the solvent. Abbreviations: OPF — Original protective film, KPF — Kapton Polyimide film, 3DC — 3D-printed cell with the CE in either i) or ii) position of Fig. 1b.

Exp. No.	Electrolyte [30 mM]	Supp. elec. [300 mM]	Solvent [50 mL]	Additives and conditions	No. of cells
PdE-001/**2**	$PdCl_2$	LiCl	H_2O/**D_2O**		3/**3**
PdE-003/**4**	$CuCl_2$	LiCl	H_2O/**D_2O**		3/**3**
PdE-005/**6**	$PdCl_2$	KCl	H_2O/**D_2O**		3/**3**
PdE-007/**8**	$PdCl_2$	LiCl	D_2O	DSA CE, thermometer -/**0.1 mM $PtCl_2$**	3/**3**
PdE-009/**10**	$PtCl_2$	LiCl/**LiCl**[a]	H_2O/**D_2O**	-/**10 mM D_2SO_4**	1/**2**
PdE-015	$PdCl_2$	LiCl	D_2O	OPF, thermometer	3
PdE-016	$PdCl_2$	LiCl	50:50 H_2O/D_2O		1
PdE-017/**18**	$PdCl_2$	LiCl	H_2O/**D_2O**	KPF	3/**3**
PdE-019	$PdCl_2$	LiCl	D_2O	Stirring	3
PdE-020/**22**	$PdCl_2$	LiCl	D_2O	KPF, 3DC(i)	3/**3**
PdE-021	$PdCl_2$	LiCl	D_2O	H-cell, DSA CE	1
PdE-023	$PdCl_2$	LiCl	D_2O[b]	H-cell	1
PdE-024	$PdCl_2$	LiCl	D_2O[b]	RE, 3DC(i)[c]	3
PdE-025/**26**	$PdNO_3$	$LiNO_3$	H_2O/**D_2O**	3DC(i)	3/**3**
PdE-027/**28**	$PdCl_2$	LiCl	H_2O/**D_2O**	3DC(ii)	3/**3**
PdE-029/**30**	$CuCl_2$	LiCl	H_2O/**D_2O**	3DC(ii)	3/**3**
PdE-031/**32**	$CuCl_2$	LiCl	H_2O/**D_2O**	1 mM $PtCl_2$, 3DC(ii)	3/**3**

[a] In PdE-010 LiCl concentration was 1 M.
[b] Volume of 30 mL with $PdCl_2$ on WE side of membrane and 30 mL without $PdCl_2$ on CE side.
[c] Two cells used old cell design and instead of Ag/AgCl RE used only a chlorinated Ag wire as RE.

Table 2
Recombination cell (RCC) and Fenton's reagent experiment codes and experimental parameters. The reaction taking place at the CR-39 surface was set by the direction of current.

Exp. No.	Dissolved species	Solvent	Duration A/B/C/D [min]	CR-39 surface reaction	*I* [mA]
RCC-01	0.3 M LiCl	H_2O	10/30/60/120	HER	−46.4
RCC-02	0.3 M LiCl	H_2O	–/30/60/120	OER	42.9
RCC-03	0.3 M LiCl	D_2O	30/120	HER	−49.6
RCC-04	0.3 M LiCl	D_2O	30/120	OER	39.2
RCC-05	0.3 M LiCl + 0.01 M ascorbic acid	H_2O	30/120	HER	−54.2
RCC-06	0.3 M LiCl + 0.01 M ascorbic acid	H_2O	30/120	OER	53.2
Fenton-01	0.1 M $FeSO_4$	H_2O	5/10	–	–
Fenton-02	0.1 M $FeSO_4$ + 0.01 M ascorbic acid	H_2O	5/10	–	–
Fenton-03	0.1 M $FeSO_4$ + 0.1 M ascorbic acid	H_2O	5/10	–	–

H_2O (Milli-Q Direct-Q, >18 MΩ cm) or D_2O (Armar Isotopes 99.8%). LiCl (VWR, ≥ 99%), KCl (VWR, 99.5%) or $LiNO_3$ (Sigma-Aldrich, 99.995%) were added as supporting electrolytes and D_2SO_4 (Armar Isotopes 98 wt%) was used as an additive in one of the experiments. Experimental parameters of PdE measurements are presented in Table 1 and chemical batch numbers and their analysis certificates are included in SI 1. One to three independent replicates were performed simultaneously (labeled *e.g.* PdE-001 A, -001B and -001C). Electrolyte samples were collected before and after the experiments. Inductively coupled plasma mass spectrometry, described in SI 2, was used to analyze changes in the isotopic contents.

The PdE measurements were performed with Landt Instruments G340 A battery cycler in constant current mode. The five-day experiment consisted of five subsequent 24 h current holds at 0.1 mA, 0.5 mA, 5 mA, 25 mA and finally 100 mA. It should be noted that due to the 5.25 V voltage limit of the battery cycler, the last current was rarely achieved. For this reason, the H-cell experiments used Peaktech 6225 A power supply instead to overcome the increased ohmic resistance. All measurements were performed on a vibration dampening surface at room temperature. Protective films were utilized to separate the CR-39 pieces from the Ag WE and the electrolyte solution in a subset of the experiments. In PdE-015, the 50 μm thick ethylene vinyl acetate (determined by FTIR measurement, see SI 3) original protective film (OPF), which is normally removed before use, was left in place. Kapton polyimide film (KPF) with 6 μm thickness was used in PdE-017/18 and PdE-020/22). In PdE-015 the cell temperature was monitored over time with a thermocouple encased in glass tube. Reference electrodes (RE) were considered for more accurate measurement of overpotentials but tests with self-made 3 M KCl Ag/AgCl reference electrodes were found to be unstable over the extended experimental durations (PdE-024) and thus not utilized in other measurements.

2.2. Recombination cell

Measurements into the hydrogen-oxygen recombination in the RCC measurements used 3D-printed PLA holders illustrated in Fig. 1c. The holders were submerged in beakers with 25 mL of electrolytes described in Table 2 along with the potential hold durations and average absolute value of current at 5.25 V potential. The reaction taking place on the slanted CR-39 piece was HER with negative currents and OER with positive currents. This design resembles Hull cell designs, where the current density (and HER reaction rate) varies along the slanted wire. Platinum wires (0.5 mm diameter Jalometallitukku Bergman 99.9%) were used as both WE and CE. Ascorbic acid (Merck) was used as the free radical scavenger. Also presented in Table 2 are the Fenton's reagent experiments where CR-39's response to OH-group radicals was tested by combining H_2O_2 (Fischer Scientific, 30%) and iron(II) sulfate heptahydrate (SCBT) with varying concentrations of ascorbic acid.

Table 3
Polymer cavitation damage (PCD) experiment solutions.

Exp. no.	Solution
PCD-01	H_2O
PCD-02	H_2O + 0.3 M LiCl
PCD-03	H_2O + 0.3 M LiCl + 1 M ascorbic acid
PCD-04	D_2O
PCD-05	D_2O + 0.3 M LiCl + 1 M ascorbic acid

2.3. Polymer cavitation damage

Ultrasound-induced cavitation was used to damage CR-39 surfaces in the PCD measurements. CR-39 pieces were submerged in different solutions described in Table 3, using the same chemicals as in earlier PdE and RCC experiments. Experiments from PCD-01 to PCD-03 used a 2 L container with ion exchanged water whereas D_2O-based PCD-04 and PCD-05 used a 3D-printed PLA container with 180 mL fluid volume. It should be noted that PCD-02 detector suffered a mishap during the etching process and was ruined.

An in-house built focusing transducer that has a bowl-shaped piezo element, and is glued with epoxy to a 3D-printed housing, was used to generate the ultrasound pulses (for more details, refer to Holmström et al. [27]). The excitation signal was generated with an arbitrary signal generator (Siglent SDG6022X) and amplified by a power amplifier (Amplifier Research, 500100 A). Electrical impedance was matched to 50 Ω at the working frequency of the piezo element at $f = 11.5$ MHz. A lower excitation amplitude was used to align the transducer, and cavitation bubbles were created using amplitudes high enough to exceed the cavitation threshold. The transducer generates a focusing acoustic field that coincides at a focal point. The transducer-to-sample distance was found by using pulse-echo monitoring (Picoscope 5444D) and by translating the transducer to a z-position where the received echo signal was maximized. This position was defined as an offset distance of z= 0 μm. In the cavitation-damage experiments, various transducer-to-sample distances were employed. The transducer was moved upward, causing the induced cavitation cloud to rise incrementally away from the surface. We hypothesized that, as the distance increases, the probability of surface erosion would decrease and the damaged area would become smaller. When the focus was found, a coarse amplitude sweep was performed to find the amplitude range that induced inertial cavitation.

After transducer alignment, high-amplitude bursts of focused ultrasound were launched for adjacent areas on the CR-39 surface. The series consisted of three repetitions of sonication at a set of increasing transducer-to-sample distances: 100 μm, 200 μm, 400 μm, 600 μm and 800 μm. The excitation signal consisted of 500 bursts (20 cycles per burst) that were launched at each spot at 100 Hz pulse-repetition frequency (PRF). The peak-to-peak voltage (U_{pp}) of the excitation outputted from the power amplifier was 300 V_{pp}.

A stroboscopic Schlieren imaging system [28] was used in PCD-01 to PCD-03 to visualize ultrasound propagation and cavitation on the surface of the CR-39 by changing the time delay between ultrasound excitation and pulsing of light source of the Schlieren imaging system.

After the experiments, the cells were disassembled and the CR-39 pieces were thoroughly rinsed with distilled water and stored in open-top glass vials and allowed to dry. Etching of the CR-39 pieces was generally performed within 24 h of the end of an experiment, with PdE-001 and PdE-002 being exceptions having been etched nearly a week later. The detectors were etched for 180 min in freshly prepared 5 M NaOH (VWR) heated to 85 °C, with etching rate of ≈ 3.04 μm h^{-1} calculated from Ishigure et al. [29]. After etching the detectors were thoroughly rinsed with distilled water, let to dry and imaged with Euromex bScope microscope. A selection of the CR-39 pieces were later imaged with Alicona InfiniteFocus G6 scanning 3D microscope using 1900 WD30 (5x magnification, 6.8 μm lateral resolution), 400 WD19 (20x, 2.3 μm), 150 WD11 (50x, 1.6 μm) and 80 WD4 (100x, 1.2 μm) objectives. Reference CR-39 samples, with and without OPF and KPF protective films, were irradiated with alpha radiation from an ^{241}Am source with 12 mm separation at right angle.

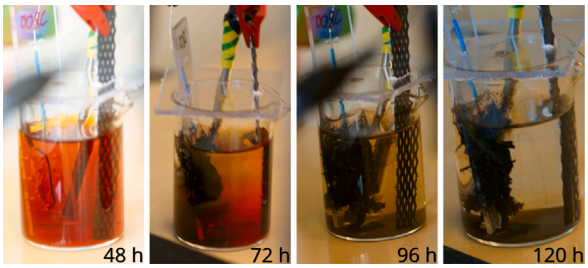

Fig. 2. PdE-008C cell imaged at different points of the five day experimental period shows that at higher currents and thus potentials the dissolved palladium deposited on the Ag wire grows dendritically towards the CE. At higher currents the gas bubbles created during HER and OER break the dendritic growth, causing palladium to accumulate at the bottom of the cell.

Pit diameters were extracted from the 3D microscope scans with Fiji software [30] using the ImageJ-Particle-detection-and-analysis macro [31]. Diameters of the pits with circularity above 0.9 were selected and plotted in histograms. COMSOL Multiphysics® software was used to simulate CR-39 etching with different initial damage dimensions. Full details of the data analysis and COMSOL simulations are given in SI 4 and SI 5 of the Supporting information, respectively.

3. Results

3.1. Pd-H/D co-deposition

Experiments on CR-39 damage during metal-hydride co-deposition were started by reproducing earlier research by P. Mosier-Boss and L. Forsley [8–10] using the experimental procedure described in [9] with the change to a shorter current profile, as described earlier in the experimental section. In PdE-001 (H_2O-based) and PdE-002 (D_2O-based), during the first 48 h with applied currents at 0.1 and 0.5 mA (0.8 and 1.0 V, respectively), Pd deposited slowly on the Ag wire, without water splitting taking place. Increasing the current to 5 mA (2.0 V) caused the remaining palladium to deposit quickly in highly dendritic fashion and the onset of HER. The dendritic palladium deposit was broken up over time due to the evolving H_2 bubbles and accumulated at the bottom of the cell. This is illustrated for PdE-008C in Fig. 2. In addition to metal deposition, hydrogen evolution, oxygen and chlorine reduction can occur at the cathode at the applied potentials. At the anode, oxygen and chlorine evolution could occur, although OER is more thermodynamically favorable [32]. Additionally, all the hydrogen arriving at the electrode would be oxidized at the anode. Moreover, oxidation of Pd(II) to Pd(IV) is possible, and was indeed observed when using KCl as the supporting electrolyte (PdE-005/6) as the formation of a poorly soluble red potassium hexachloropalladate(IV) layer on the anode.

The CR-39 etching process amplifies any local damages to microscopic dimensions, which were then imaged with a scanning 3D microscope. Fig. 3 presents composite images acquired with focus-variation scanning 3D microscope, for experiments carried in H_2O (Figs. 3a & 3b) and D_2O (Figs. 3c & 3d). Broad streak-like background features originate from the composite rendering and surface residues, and are not included as pits in the analysis. It can be seen that both detectors exhibit highly circular pits with peaks in diameter distribution at around 5 μm, 10 μm and 25 μm, as shown in Fig. 4. Peak positions and their standard deviations for the analyzed detectors are presented in Table 4.

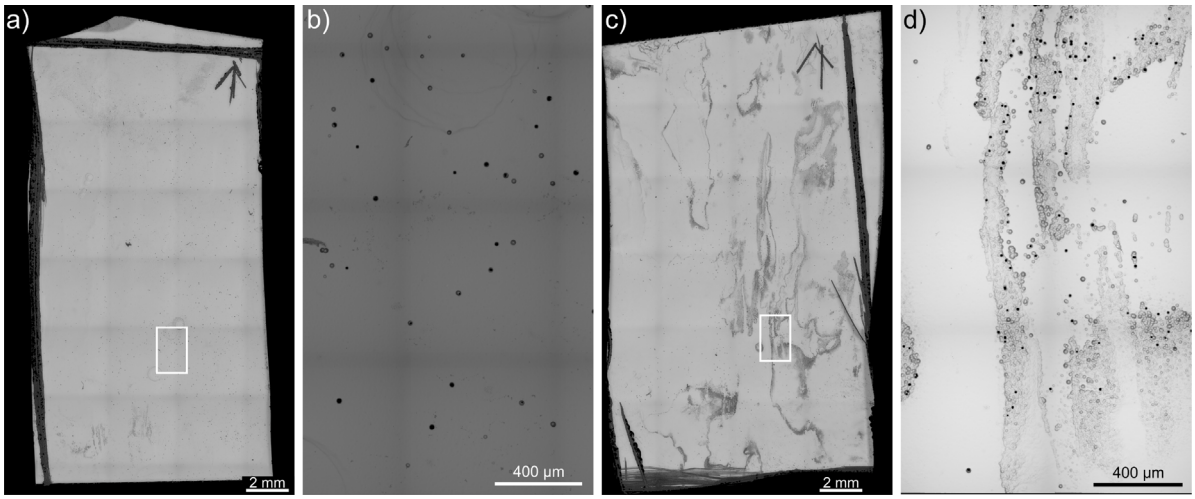

Fig. 3. Scanning 3D microscope images of detectors etched after the five day Pd-H/D co-deposition experiments. (a) With H_2O-based electrolyte in PdE-001 A, the detector shows hardly any large scale patterns, only individual pits spread sporadically over the entire detector surface with the white rectangle marking the close-up in (b), which shows relatively uniform circular pits. (c) In D_2O-based PdE-002B largest pit densities were observed near the Ag WE position during the co-deposition experiment. (d) Pits seen in the close-up of the indicated area of interest are more varied in size and form regions with multiple overlapping pits. For some pits, the microscope was not able to resolve the bottom depths and those pixels register as black.

The smaller 5–10 µm pits were observed in significantly higher densities in cells with D_2O-based electrolytes and these pits were mostly concentrated in the immediate vicinity of the Ag WE. On the other hand, the pits with the largest 25–26 µm diameters exhibited no such spatial coordination with respect to the working electrode. These tracks are thought to have originated from background radiation during the multi-day period after the experiments conclusion but before the detectors were etched. This is supported by the fact that similar tracks were observed in control CR-39 pieces (PdE-001/2-control and PdE-006/010-control) that were only submerged in deionized H_2O during the experimental period, indicating that the contamination likely arises from natural radon decay background. Alpha particles originating from ^{222}Rn decay have similar energies (5.59 MeV) to ^{241}Am, which were used to calibrate CR-39 alpha response and, as seen in Fig. 5, produce similar tracks with average diameters of 26.6 µm. In Finland average radon background is around 100 Bq/m^3 [33]. After this contamination was noted, the subsequent experiments were etched within 24 h after the experiment's conclusion, which resulted in near complete elimination of these tracks. In order to verify the PdE-001 and PdE-002 experiments, additional replication experiments were performed at Technical University of Munich and Aalto University. These experiments summarized in SI 7 and SI 8, confirm the reproducibility of presented results.

Dissimilarity of pit quantity and spatial distribution with respect to the working electrode indicated that the use of heavy water as the solvent has considerable effects on the pit formation. The effect of various system parameters on pit formation were investigated in experiments listed below with the initial result being that pits similar to Fig. 3b were only observed when co-depositing palladium and deuterium.

Tested variations of the base experiment:

- Substituting $PdCl_2$ with $CuCl_2$ (PdE-003/4) or $PtCl_2$ (PdE-009/10) as the active species.
  Result: No pits observed
  Conclusion: Pd is required in the system to observe pits.
- Eliminating lithium from the system by substituting LiCl with KCl (PdE-005/6).
  Result: Pits observed
  Conclusion: Lithium is not necessary to pit formation.
- Removing chlorine from the system by replacing $PdCl_2$ and LiCl with $PdNO_3$ and $LiNO_3$ (PdE-025/26).
  Result: Pits observed
  Conclusion: Presence of chlorine does not affect pit formation.
- Removing Pt from system by the use of DSA CE (PdE-007/8).
  Result: High concentrations of pits observed
  Conclusion: Pt is not required to form pits, CE surface area possible affects the number of pits observed.
- Mixing H_2O and D_2O in one-to-one ratio.
  Result: Pits observed
  Conclusion: Presence of light water does not prevent bubble formation.

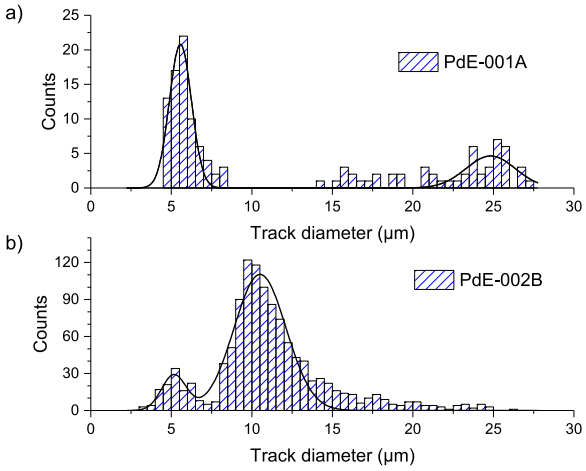

Fig. 4. Diametral distribution of (a) H_2O-based PdE-001 A and (b) D_2O-based PdE-002B both show pits in 5–10 µm range and in the 25 µm range indicative of radon background exposure.

Additional experiments suggested in [9] to exclude non-nuclear pit sources were tested. When the 50 µm thick original CR-39 protective film was left in place (PdE-015) or a 6 µm thick polyimide film was added (PdE-017/18 and PdE-020/22), pits were not observed in areas where the film separated the CR-39 surface from the electrolyte, only at places where the film had come loose at the detector edges, one example is presented in Figure S7. In another experiment forced convection was applied to the electrolyte by a magnetic stirrer (PdE-019). In this experiment it was observed that Pd deposited much closer to the Ag wire as the dendritic growth was suppressed and pits were found

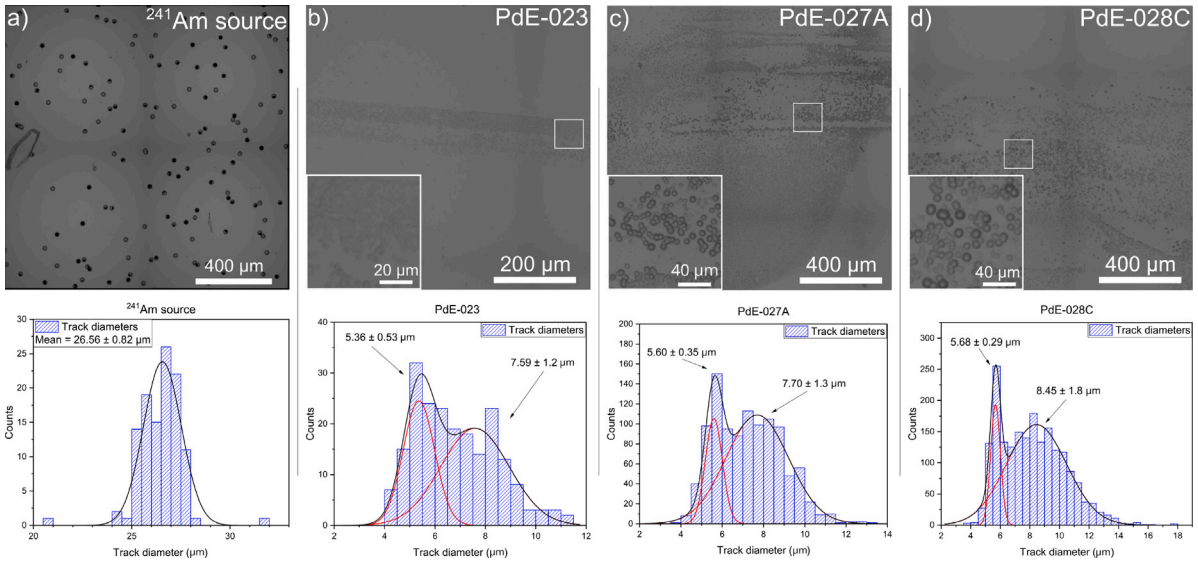

Fig. 5. Images of selected subsections of analyzed regions of interest and the pit diameter distributions fitted with normal distributions. White squares outline the regions shown in the insets at greater magnification. (a) Etched tracks after ^{241}Am exposure. Due to the small size of the pit bottoms, the depth of the deepest pixels could not be recorded and as such they register as black pixels. (b) Pits produced in the H-cell experiment. Pits produced in (c) H_2O-based and (d) D_2O-based experiments where CE was situated underneath the WE.

only in the immediate vicinity of the Ag wire indicating that proximity of metallic Pd was a prerequisite for pit formation at a specific area. Time evolution of the electrolyte temperature was measured in PdE-007/8 and PdE-015 to see if additional heating would be observed but the cell temperatures evolved in line with ohmic heating and expected day-to-day variation.

3.2. Recombination and radicals

With these observation in mind, we started considering alternative mechanisms that might cause the localized CR-39 pits. Explosive recombination of oxygen and hydrogen gasses produced during the electrolysis has been suggested as the source of the damage [21]. This was investigated first by using an H-cell (PdE-021 and PdE-023) where the HER and OER/ClER reactions were spatially separated into their respective cell halves connected by a cation exchange membrane. Pits from PdE-023 cell shown in Fig. 5 present similar diameter distributions with respect to the previous experiments but were restricted to the region directly beneath the Ag wire as opposed to its sides as in earlier experiments with similar pits. 3D-printed cell design depicted in Fig. 1c was used in the RCC measurements to examine if the mixing of H_2/D_2 and O_2 gasses during water splitting would be able to damage the CR-39 surface and if the spatial separation of working and counter electrodes had any effect on the observed damage. However, due to the high HER and OER rates, the CR-39 surface was quickly saturated with macroscopic bubbles increasing the ohmic resistance and shielding the CR-39 surface from interactions with gas evolved at the counter electrode. Damage observed in these cells was only thermal in nature and characterized by large smooth surface gradients in the etched detectors located directly below the Pt WE. Free radicals were also considered as a possible source for the initial damage on CR-39 surfaces. When CR-39 was exposed to •OH and HOO• radicals generated with Fenton's reagent, with or without ascorbic acid, serving as a free radical scavenger [34], no damage was observed. This result was used to rule out radicals as the damage source. The reader is referred to SI 9 for further details.

However, it was later found that neither Pd or D_2O was necessary for pit formation. In co-deposition experiments where the counter electrode was placed underneath the working electrode, position (ii) in Fig. 1b, pits could be produced in either aqueous isotope (PdE-027/28), as presented in Fig. 5. Simply substituting Pd for Cu (PdE-029/30) did not produce pits but when 1 mM $PtCl_2$ (PdE-031/32) was added to catalyze HER during Cu-H/D co-deposition, pits could again be observed. These pits and their diameter distributions are shown in S8. In conclusion, instead of being specific to Pd-D co-deposition, pit formation seemed to mostly depend on the HER activity of the deposited metal.

3.3. Acoustic cavitation erosion

In order to compare the CR-39 response to a known cavitation source, high-intensity focused ultrasound method was used to induce ultrasound cavitation bubbles in the vicinity of the polymer surface. Naturally, ultrasound cavitation bubbles differ from the electrochemically produced bubbles, but literary sources suggest that bubbles behave largely similarly once created without being dependent on the specific formation mechanism [35,36]. A mostly qualitative comparison of the ultrasound cavitation bubbles and electrochemically generated bubbles should be reasonable. In ultrasound cavitation, ultrasound pulses coincide at a focal point resulting in such pressure gradients that a cloud of imploding cavitation bubbles is formed. When this takes place near a boundary, collapsing cavities produce microjets that impact the surface, damaging it. Using Schlieren imaging, the propagation of the ultrasound pulses and the resulting cloud of cavitation was recorded for visualization purposes, as shown in Fig. 6a. The CR-39 pieces accrued visible damage even before etching took place, especially at the area used to align the transducer at the focus and sweep over different amplitudes. Therefore, more surface erosion occurred near this spot as the same region was constantly sonicated (at the given PRF) over an extended period of time. This area is outlined with a red square on the top left corner of the etched detector shown in Fig. 6b. The pits produced by the used excitation parameters (20 cycles/burst, 500 bursts at PRF = 100 Hz), at different transducer offsets are also shown in the same image. Assuming that a single pit (having 6 µm diameter after etching) is produced by one cavitation-collapse event, the dimensions of the individual pits do not change with the transducer offset. However, the total number and extent of the pits at each sonication site appear to be inversely proportional to the offset distance. There are only a limited number of individual cavitation bubbles that were formed in sufficient proximity to the CR-39 surface, mostly directly below the bubble cloud, to damage it. In all PCD experiments, the pits produced by ultrasound cavitation were

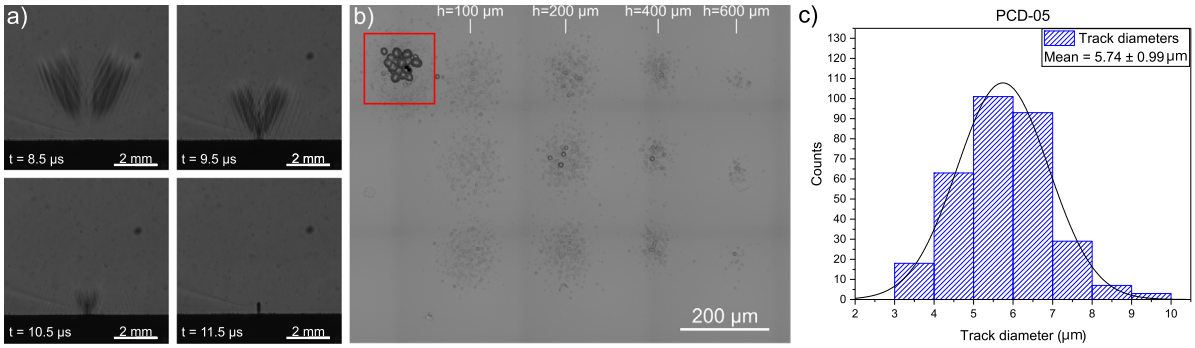

Fig. 6. (a) Shows images of ultrasound wave propagation in PCD-03 toward the CR-39 surface (time delay from 8.5 µs to 10.5 µs) and the resulting generation of a cavitation cloud near the surface in the last frame (time delay 11.5 µs). The transducer offset was 600 µm upwards from the focus zero. (b) Pits seen in PCD-05 produced by cavitation at different heights after etching. Pits at the top left corner (red square) were produced during the transducer alignment and initial amplitude sweep to find out the suitable excitation amplitude for cavitation generation. (c) Pit diameter distribution after etching for pits produced at all focal point offsets averages at around 5.7 µm diameter.

highly circular and their diameters were normally distributed at around 6 µm on average, shown for PCD-05 in Fig. 6c (for other experiments, the peak positions and their standard deviations are reported in Table 4). The diameters of individual cavitation pits being independent of the transducer offset indicates that the cavitation damage accrued by CR-39 is more dependent on the characteristics of the cavitation events themselves, and as such, different pit diameters could be produced by altering the frequency used to generate them from the used 11.5 MHz frequency corresponding to 0.6 µm Minnaert resonance bubble size. Compared to the co-deposition experiments, pits produced by ultrasound-induced cavitation are closely in the same diameter range but without exhibiting the bifurcation of the diametral distribution, which indicates the possibility of multiple types of cavitation events in the co-deposition systems.

3.4. Pit depths

In addition to the pit diameters, the penetration of the pits observed in the co-deposition and cavitation experiments into the CR-39 surface was evaluated by examining the distribution of 3D-scanned points by their z-coordinates, *i.e.* depth and compared to tracks produced by an ^{241}Am source. Fig. 7 depicts the relative abundance of points at specific depths from the zero-plane of the imaged detector surface. In our detectors, the tracks produced by alpha sources in the 5.5 MeV energy range, ^{241}Am (cf. Fig. 5a) and ^{222}Rn for the presumed background tracks (tracks around 25 µm diameters in PdE-001 A cf. Fig. 3b), penetrate up to 20 µm deep into the CR-39 surface. Comparable penetration depths at 30–35 µm are reported in literature [37,38]. These tracks are considerably deeper than the pits observed near the Ag WE in the Pd-H/D co-deposition experiments or in the ultrasound cavitation experiments. After 180 min of etching their pits show residual depths of less than 2 µm relative to the etched surface. These values should not be interpreted as the original latent damage depths before etching, rather as the combined effects of bulk etching and preferential etching of the damaged surface. Additionally, it should be noted that the deepest points of the ^{241}Am-produced tracks could not be recorded due to the optical limits imposed by the visible light wavelengths and because of that the true alpha particle track depths are deeper than the ~ 22 µm depths presented in Fig. 7.

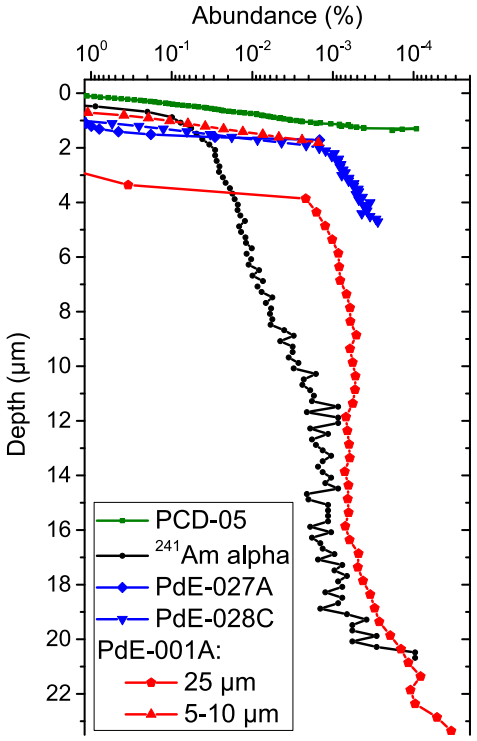

Fig. 7. Relative abundance of 3D-scanned points at various depths. Tracks produced by ^{241}Am source and the 25 µm diameter radon tracks in PdE-001 A (25 µm diameter) penetrate significantly deeper than the pits observed near the Ag WE in co-deposition experiments (PdE-001 A (5–10 µm diameter), PdE-027 A and PdE-028C) or ultrasound cavitation (PCD-05).

4. Discussion

A few key insights can be highlighted from the results. Pits are observed on CR-39 surfaces during metal-hydride/deuteride co-deposition when HER takes place in its proximity, and this seems to be more easily observed in D_2O-based electrolytes. These pits occur in clusters and are spatially coordinated with the working electrode and their occurrence increased when the CE was placed such that oxygen/chlorine bubbles were present in the general vicinity of the CR-39 detector surface. Pit diameters are normally distributed and, in most cases, split into two peaks, one at 5–6 µm and another at 8–10 µm. Ratio of the peak positions, *e.g.* $\frac{5.46\,\mu m}{10.7\,\mu m} = 0.510$ for PdE-001 A, was on average 0.61 in experiments where two peaks were observed. Pits with similar diameters (without bifurcation) were obtained when CR-39 was subjected to cavitation caused by high-intensity focused ultrasound. It would be unlikely that these pits are the result of CR-39 exposed to energetic particles created in a nuclear reaction during the metal-H/D co-deposition and water electrolysis, as tracks produced by an ^{241}Am source were significantly larger (26–27 µm diameter) and considerably deeper. Alternative reactions that would produce alpha particles during

Table 4
Peak positions and standard deviations of the normal distributions fitted to the histogram data of the experiment replicates.

	Replicate A	Replicate B	Replicate C
Exp. No.	$\overline{d}$ [μm]	$\overline{d}$ [μm]	$\overline{d}$ [μm]
PdE-001	5.46 ± 0.43, 10.7 ± 1.7	8.56 ± 1.5	5.65 ± 0.62
PdE-002	–	5.16 ± 0.65, 10.5 ± 1.4	5.59 ± 0.49, 10.3 ± 1.4
PdE-006	6.87 ± 1.2	5.21 ± 0.88	5.04 ± 0.44, 7.97 ± 1.8
PdE-023	4.94 ± 0.69	–	–
PdE-027	5.60 ± 0.35, 7.70 ± 1.3	5.56 ± 0.60	5.50 ± 0.33, 7.65 ± 1.3
PdE-028	7.35 ± 1.3	7.38 ± 1.5	5.68 ± 0.29, 8.45 ± 1.8
PdE-031	5.39 ± 0.65, 9.16 ± 1.1	–	–
PdE-032	–	4.56 ± 0.48	4.58 ± 0.73
PCD-01	6.49 ± 0.53	–	–
PCD-03	5.09 ± 0.99	–	–
PCD-04	6.55 ± 0.84	–	–
PCD-05	5.74 ± 0.99	–	–
KPF	16.3 ± 0.48	–	–
OPF	4.43 ± 0.33	–	–
^{241}Am	26.56 ± 0.82	–	–
PdE-006/010-control	14.9 ± 1.1	–	–

electrolysis with two distinct energies are not supported by existing fusion pathways [39]. Furthermore, some sources [40–42] suggest that various transmutations of Pd nuclei could take place during the Pd-D co-deposition. ICP-MS analysis of electrolyte samples taken before and after the experiments showed no statistically significant changes from the natural Pd isotope ratio. No traces of transmuted elements such as Ru or Ag were detected. For further details, see SI 2. With respect to the alternative non-nuclear mechanisms, OH-group radicals can be dismissed as a cause, as exposure to Fenton's reagent failed to produce damage of this type all together, leaving cavitation as the most probable source of observed damage.

Nanoscopic hydrogen and oxygen bubbles are generated during HER/OER [43] and proceed to merge into larger bubbles. These microscale bubbles typically rest on a "carpet" of nanobubbles and grow as more nanobubbles coalesce into them. Upon reaching a critical size, the surface microbubbles detach and escape into the bulk medium as spherical bubbles [44–46]. Hemispherical surface hydrogen nanobubbles created during HER have been reported to have average radii of 42 nm at −1.1 V and 90 nm at −2.0 V vs. Pt RE, indicating that higher overpotentials lead to larger nanobubbles [47]. Guo et al. [48] recently reported directly observing sub-50 nm diameter surface nanobubbles during electrolysis with similar dependency on overpotential. Bulk hydrogen nanobubbles have been reported in around 200 nm diameter range [49]. Bifurcation of the pit diameter distribution observed in our detectors could be explained by the different damage profiles originating from cavitation of spherical nanobubbles and high contact angle (HCA) surface nanobubbles within the hydrogen nanobubble carpet. Micro- and nanojets are produced during a cavitation event as the flow of fluid rushing in to fill the void of a cavitation bubble is impeded by nearby solid surfaces, which results in the far side of the bubble collapsing faster and thus producing a net flow, *i.e.*, a jet, of liquid toward the surface [50]. When nanobubbles collapse spontaneously in ambient pressures, they do not generally produce jets as viscosity effects dominate at these length scales [51,52]. Jetting behavior, however, is expressed in such systems when a short range water hammer effects or arc-shaped shock waves arising from collapse of nearby bubbles [53,54], interact with the nanobubbles and cause them to collapse. In computational studies by Dockar et al. [24], shock-induced collapse of nanobubbles was shown to produce pits on solid substrates, such as on amorphous silicon, with the resulting pit diameters being very close to the projection, *i.e.*, the shadow of the initial bubble on the surface [55]. This applies to both collapses of spherical and surface nanobubbles, but the depth of the resulting damage is significantly affected by the bubble type. When spherical nanobubbles collapse, they generally have time to fully form their jets and thus produce deeper damage profiles. Especially, the outflow of the fluid after the initial jet "punch" exacerbates the removal of substrate material. Jets produced during the collapse of HCA surface nanobubbles impact the substrate before reaching their maximum jet velocities. As a result, the pit has a similar diameter to the spherical nanobubble collapse pit, but are considerably shallower, at around a third of their depth, partly due to the elimination of fluid outflow.

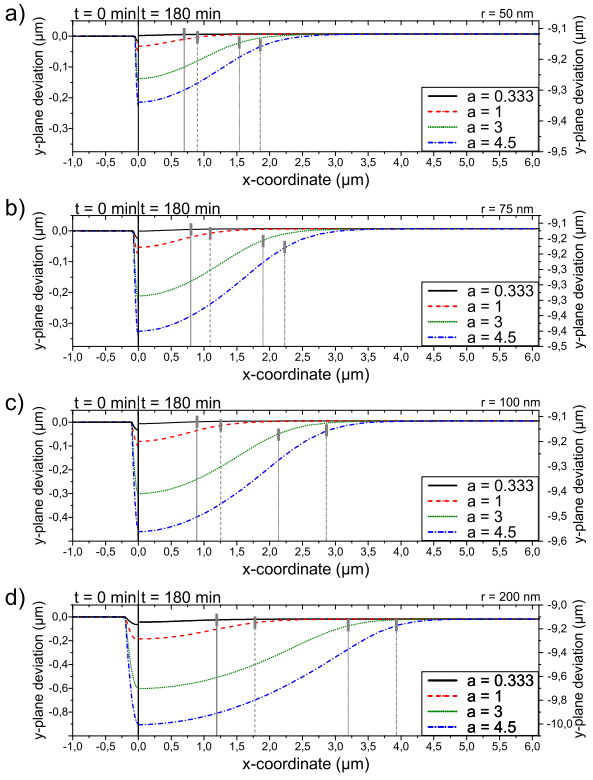

Fig. 8. CR-39 surface profiles before etching (t = 0 min) and after etching (t = 180 min) for initial surface pit radii of (a) 50 nm, (b) 75 nm, (c) 100 nm, and (d) 200 nm. Depth of the initial pit was controlled by changing the factor *a* of the quadratic equation. Pit edges were chosen as the points of maximum curvature change along the surface profile, marked with gray vertical lines. Relative dimensions of the initial seed damages are preserved over the etching process.

Alternatively, it has been suggested that oxygen and hydrogen nanobubbles can merge into oxyhydrogen bubbles with close to stoichiometric ratios of both gasses, which proceed to spontaneously combust. Resulting vapor clouds expands to micrometer scale before rapidly collapsing due to the external liquid pressure. The collapse of

the vapor bubble can directly produce microjets or alternatively it can induce the formation of secondary rebound cavitation bubbles [22,23,56]. Merging of hydrogen and oxygen bubbles into oxyhydrogen bubbles is favored over merging of two bubbles of the same gas. These oxyhydrogen bubbles are known to ignite spontaneously in a surface-assisted combustion reaction. This spontaneous ignition has been suggested to originate from dissociation of H_2 molecules into atomic hydrogen at active sites formed by surface charges [57]. As the ignition is not directly catalyzed by the co-deposited metal, it seems that the overall HER activity is more relevant and would explain why pits were observed during Cu deposition only when Pt was added to the electrolyte to better catalyze HER [23]. This reaction would be a reasonable explanation as to why the pits were observed more readily once the CE was placed underneath the WE thus allowing for mixing of the generated oxygen and hydrogen gasses. Spontaneous combustion of oxyhydrogen, however, is unlikely to be the source of the initial damage on the CR-39 surface because pits were still observed in H-cell experiments where the OER side of the cell was separated from the WE and thus hindered the mixture of hydrogen and oxygen gasses. Nevertheless, it is worth to note that Nafion is slightly permeable to oxygen [58], so, presence of small amounts of oxygen/chlorine in the cathode chamber cannot be excluded and could results in Pd-catalyzed combustion of H_2 and O_2/Cl_2, resulting in cavitation damage.

It is difficult to estimate the dimensions of the initial damage caused by cavitation on the CR-39 surface. In the computational works involving amorphous silicon, with its 5.5 GPa ultimate tensile strength, the maximum pit depths were below 10 nm. It would be expected that the pit depths were noticeably deeper due to its sub-100 MPa tensile strength [59], as material hardness has been linked to material's cavitation erosion resistance [60]. Cavitation has been shown to mechanically damage Pt, Pd, Au, Ti and W electrodes during pulsed water electrolysis with alternating polarity, where harder electrode materials proved more resistant toward cavitation damage [22,23,56]. On the other hand, highly malleable Au is considerably more resistant toward erosion than aluminum [27], even if they have similar hardnesses [61], and compared to Au, CR-39 is quite brittle [62]. Spherical nanobubbles are expected to produce initial damage pits with diameters similar to its radius R with pit depths scaling linearly with R. HCA nanobubbles, on the other hand, produce pits with diameters similar to the radius of the bubble base R_{base} but with constant depths [24]. This could offer an explanation to the observe track diameter distribution bifurcation; both HCA and spherical nanobubbles are present on the CR-39 generated during the HER reaction on the nearby metal deposits, which collapse via cavitation and produce seed damage pits with roughly identical diameters but with different depths. Deeper pits are etched more strongly resulting in larger pit diameters.

COMSOL Multiphysics simulations were used to validate that differences in the initial seed damage dimensions are preserved during the etching process. Fig. 8 shows the initial pits with seed damage radii $R_{seed} = 50\text{ nm},\ 75\text{ nm},\ 100\text{ nm},\ 200\text{ nm}$ at $t = 0$ min and pits post-etching at $t = 0$ min. Seed damages were given a quadratic shape $y(x) = ax^2 + c$ with a boundary condition $y(x \geq R_{seed}) = 0$, giving linear relationship between a and maximum pit depth c. Four different factors a were chosen to represent different initial pit depths ($a = 0.333,\ 1,\ 3,\ 4.5$). Due to the low surface gradients, like in optical microscopy, specific surface angles could not be used to determine the pit edges, and thus they were chosen to reside at the points of maximum curvature change, instead. It is apparent that deeper seed damages produce wider pits and preserve their shape better during the etching process. When comparing pits with the same R_{seed} at one-to-three depth ratios in Fig. 8, it can be seen that ratio of pit radii *e.g.* at 200 nm $\frac{a_{0.33}}{a_1} \approx 0.68$ and $\frac{a_1}{a_3} \approx 0.55$, are similar to the diameter distribution peak ratios observed during the co-deposition experiments. This supports the argument that diametral distribution peak bifurcation is the result of cavity collapse of two different nanobubble types. More details on the COMSOL simulations and replication instructions can be found in the Supporting information SI 5 and SI 6.

Dockar et al. had observed that while HCA and spherical nanobubbles produces pits with similar diameters on the substrate during cavitation collapse, pits produced by surface bubble collapse were roughly one third as deep. For our system, this provides a potential physical explanation for the two pit-diameter modes. Our etching simulations show deeper seed damages evolving into wider pits, suggesting that the initial bimodal damage-depth distributions are preserved in the pit diameter distribution during the etching process. This conclusion, however, is admittedly relatively qualitative interpretation of the observed results rather than a direct identification of the damage processes.

The origin of differences in pit formation between the two aqueous isotopes need to be considered. Literary sources on heavy water electrolysis are rather limited, and, *e.g.*, bubble dynamics of D_2 gas during deuterium evolution reaction have not been thus far investigated to our knowledge making direct comparison between H_2O and D_2O nanobubble cavitation difficult. One possibility is the slower growth and subsequent detachment of D_2 gas bubbles. HER reaction rate k is faster in H_2O due to kinetic isotope effect, and the ratio of the two isotopes k_H/k_D increases with polarization [63]. Slower gas evolution in D_2O at higher overpotentials could enable higher surface coverages and more nanobubble mergers due to the higher bubble residence time as a result of the slower bubble growth rate and detachment when compared to H_2O. Furthermore, the surface tension of evolved bubbles has been shown to be proportional to the bubble lifetime before detachment and larger detachment radii with an additional dependency on anion concentration and type in solution [64]. Static surface tension difference between H_2O and D_2O is negligible, but in dynamic systems, which evolving nanobubbles must be considered, the dynamic surface tension might behave differently between the solvent isotopes, especially when noting that the viscosity of heavy water is around 20% higher than for light water [65,66]. Further investigation of bubble dynamics in D_2O are required for qualitative comparison of these cavitation effects. Additionally, more quantitative information on the characteristics of surface damages could be examined by utilizing a multi-step etching procedure, altering between controlled etching and microscopic observation. In multi-step etching, the evolution of pit/track shape and dimensions, *e.g.* the change of elliptical pits towards a circular shape, enables more precise separation of different types of initial damages due to the different growth rates, such as diameter or depth over etching time, of damages with different origins over the etching process [67]. Commonly, the etching process is halted by thorough rinsing with distilled water [68,69], which is possibly followed by neutralizing the residual hydroxide with a weak acid [70,71], after which microscopic observations can be performed. After imaging the etching process is continued by immersing the detectors into the etchant solution. Typically, the detectors are imaged after every 30 min of etching [70]. The bulk etch rate can be calculated from measured weight loss of the detector piece after each etching step [72].

5. Conclusions

This work began by reproducing experiments onto CR-39 pit formation during co-deposition of palladium and deuterium based on earlier research. Initially, pits could only be consistently observed when co-depositing palladium and deuterium, but by promoting gas bubble interactions, pits were found in cells without deuterium and/or palladium. It was also noted that tracks produced by alpha particles penetrated an order of magnitude deeper into the CR-39 surface than pits produced in electrochemical cells. Possible non-nuclear sources for these pits were considered and cavitation phenomena was concluded to be their most likely originator. Direct cavitation collapse of either spherical or high contact angle surface hydrogen nanobubbles at the sites of deposited metal during HER is a reasonable, yet qualitative

explanation for the bifurcation of pit diameter distributions. The differences in initial damage are preserved during the etching process. Pits produced via ultrasound cavitation exhibited no diametral distribution peak splitting because cavities formed in ultrasound cavitation are spherical in nature when distant from the surface, and only a limited number of non-spherically collapsing bubbles are expected to form directly on the surface, thus resulting in mainly one type of bubble collapse. Possible explanations on why pits were initially observed more prevalently in D_2O-based electrolytes include slower bubble growth rate during deuterium evolution reaction and viscosity-related effects. Literature on D_2 gas bubble dynamics is, however, limited. Based on these findings, it could be concluded that CR-39 is not damaged due to metal-hydride co-deposition but rather due to cavitation effects taking place in the vicinity of CR-39 surface during HER. Cavitation during HER should be considered in future works involving CR-39. Computational simulations as well as more quantitative approaches into the exact nature of CR-39 response to cavitation should be considered in future research. While these findings are largely qualitative in nature, with further research into the CR-39 response to HER conditions provide a potential application for use of CR-39 in electrolyzer research to detect and characterize individual cavitation events during HER. Due to its function as an integrating detector, it could allow cavitation-related degradation characterization over extended experimental durations without the need of complex optical or acoustic measurement setups.

CRediT authorship contribution statement

Kimmo Pyyhtiä: Writing – review & editing, Writing – original draft, Visualization, Validation, Software, Methodology, Conceptualization. **Jerzy J. Jasielec:** Writing – review & editing, Software. **Tom Sillanpää:** Methodology, Investigation. **Jere Hyvönen:** Investigation. **Rainer Götz:** Validation. **Lilian Moumaneix:** Validation. **Vincent Martin:** Investigation, Formal analysis. **Arnaud Viola:** Investigation, Formal analysis. **Frédéric Maillard:** Supervision, Resources. **Tanja Kallio:** Supervision, Resources. **Ari Salmi:** Supervision, Resources. **Elena Gubanova:** Validation, Supervision, Investigation. **Aliaksandr Bandarenka:** Validation, Supervision, Resources. **Pekka Peljo:** Writing – review & editing, Supervision, Project administration, Methodology, Funding acquisition, Conceptualization.

Declaration of competing interest

The authors declare that they have no known competing financial interests or personal relationships that could have appeared to influence the work reported in this paper.

Acknowledgments

This work was supported by funding provided from the European Union's Horizon 2020 research and innovation program under grant agreement HERMES No 952184. J.J. thanks HEMS project funded by City of Salo and University of Turku. We would also like to thank Axi Holmström from University of Helsinki for her assistance with ultrasound cavitation experiments. Eter Tourunen, Inka Väisänen and Antti Salminen from University of Turku are acknowledged for enabling the 3D microscope imaging. We thank Jenna Hannonen, Jenni Jarju and Pia Damlin from University of Turku for their help in measuring the FTIR spectrum of CR-39 protective films. Finally, we would like to thank Rustem Nizamov from University of Turku for his 3D-printing expertise. Materials Analysis and Research Infrastructure (MARI) of the University of Turku was utilized in this work.

Appendix A. Supplementary data

Supplementary material related to this article can be found online at https://doi.org/10.1016/j.jelechem.2026.120104.

References

[1] Ruwiadah Tarek, Sala Sami, CR-39 nuclear track detector: A review article, Int. J. Appl. Sci. Technol. 7 (2025) 19, http://dx.doi.org/10.47832/2717-8234.23.5.

[2] A.F. Saad, N.M. Al-Faitory, R.A. Mohamed, Study of the optical properties of etched alpha tracks in annealed and non-annealed CR-39 polymeric detectors, Radiat. Phys. Chem. 97 (2014) 188–197, http://dx.doi.org/10.1016/j.radphyschem.2013.11.021.

[3] M.I. Al-Jarallah, et al., Investigation of proton response of CR-39, Nucl. Instrum. Methods Phys. Res. Sect. B: Beam Interactions Mater. Atoms 73 (4) (1993) 507–511, http://dx.doi.org/10.1016/0168-583X(93)95833-Q.

[4] Matiullah, et al., A review of the use of CR-39 track detector in personnel neutron dosimetry and spectrometry, Nucl. Instrum. Methods Phys. Res. Sect. B: Beam Interactions Mater. Atoms 51 (1) (1990) 76–84, http://dx.doi.org/10.1016/0168-583X(90)90542-3.

[5] G.S. Sahoo, et al., Effects of neutron irradiation on optical and chemical properties of CR-39: Potential application in neutron dosimetry, Appl. Radiat. Isot. 94 (2014) 200–205, http://dx.doi.org/10.1016/j.apradiso.2014.08.012.

[6] Hirokazu Miyoshi, et al., Optical property of CR-39 synthesized by doping with methylviologen-encapsulated SiO2 nanocapsules as a solid-state X-ray plate detector, Opt. Mater. 55 (2016) 109–114, http://dx.doi.org/10.1016/j.optmat.2016.02.042.

[7] Stanislaw Szpak, Pamela Boss, Frank Gordon, Further evidence of nuclear reactions in the Pd/D lattice: Emission of charged particles, Naturwissenschaften 94 (2007) 511–517, http://dx.doi.org/10.1007/s00114-007-0221-7.

[8] P.A. Mosier-Boss, et al., Detection of high energy particles using CR-39 detectors part 1: Results of microscopic examination, scanning, and LET analysis, Int. J. Hydrog. Energy 42 (1) (2017) 416–428, http://dx.doi.org/10.1016/j.ijhydene.2016.09.223.

[9] Pamela Boss, Lawrence Forsley, Energetic particle emission in Pd/D Co-deposition: An undergraduate research project to replicate a new scientific phenomenon, J. Lab. Chem. Educ. 6 (2018) http://dx.doi.org/10.5923/j.jlce.20180604.01.

[10] P.A. Mosier-Boss, L.P. Forsley, Chapter 2 - Review of Pd/D Co-deposition, in: Jean-Paul Biberian (Ed.), Cold Fusion, Elsevier, ISBN: 978-0-12-815944-6, 2020, pp. 17–36, http://dx.doi.org/10.1016/B978-0-12-815944-6.00002-6.

[11] Phillip J. Smith, Robert C. Hendricks, Bruce M. Steinetz, Electrolytic co-deposition neutron production measured by bubble detectors, J. Electroanal. Chem. 882 (2021) 115024, http://dx.doi.org/10.1016/j.jelechem.2021.115024.

[12] Kuo-Yi Chen, et al., Electrochemical loading enhances deuterium fusion rates in a metal target, Nature 644 (8077) (2025) 640–645, http://dx.doi.org/10.1038/s41586-025-09042-7.

[13] Adolphe Chapiro, Chemical modifications in irradiated polymers, Nucl. Instrum. Methods Phys. Res. Sect. B: Beam Interactions Mater. Atoms 32 (1) (1988) 111–114, http://dx.doi.org/10.1016/0168-583X(88)90191-7.

[14] L. Calcagno, G. Compagnini, G. Foti, Structural modification of polymer films by ion irradiation, Nucl. Instrum. Methods Phys. Res. Sect. B: Beam Interactions Mater. Atoms 65 (1) (1992) IN7–422, http://dx.doi.org/10.1016/0168-583X(92)95077-5.

[15] T. Yamauchi, et al., Formation of CO2 gas and OH groups in CR-39 plastics due to gamma-ray and ions irradiation, Radiat. Meas. 36 (1) (2003) 99–103, http://dx.doi.org/10.1016/S1350-4487(03)00102-1, Proceedings of the 21st International Conference on Nuclear Tracks in Solids.

[16] Donald A. Tryk, et al., Mechanisms for the production and suppression of hydrogen peroxide at the hydrogen electrode in proton exchange membrane fuel cells and water electrolyzers: Theoretical considerations, Catalysts 14 (12) (2024) http://dx.doi.org/10.3390/catal14120890.

[17] M. Zatoń, J. Rozière, D.J. Jones, Current understanding of chemical degradation mechanisms of perfluorosulfonic acid membranes and their mitigation strategies: a review, sustain. Energy Fuels 1 (2017) 409–438, http://dx.doi.org/10.1039/C7SE00038C.

[18] Eva Wallnöfer-Ogris, et al., Main degradation mechanisms of polymer electrolyte membrane fuel cell stacks – Mechanisms, influencing factors, consequences, and mitigation strategies, Int. J. Hydrog. Energy 50 (2024) 1159–1182, http://dx.doi.org/10.1016/j.ijhydene.2023.06.215.

[19] F.A. de Bruijn, V.A.T. Dam, G.J.M. Janssen, Review: Durability and degradation issues of PEM fuel cell components, Fuel Cells 8 (1) (2008) 3–22, http://dx.doi.org/10.1002/fuce.200700053.

[20] Anupam Ghosh, Tinku Sharma, Jay Pandey, Review on proton conducting membrane for PEM water electrolyser: A sustainable approach for green hydrogen production, J. Electroanal. Chem. 993 (2025) 119286, http://dx.doi.org/10.1016/j.jelechem.2025.119286.

[21] Micah Karahadian, Austin Smith, Investigation of track formation in CR-39 for various hydrated environments, 2020, http://dx.doi.org/10.13140/RG.2.2.34005.86244.

[22] Vitaly B. Svetovoy, et al., Explosion of microbubbles generated by the alternating polarity water electrolysis, Energies 13 (1) (2020) http://dx.doi.org/10.3390/en13010020.

[23] Ilia V. Uvarov, et al., Highly energetic impact of H2 and O2 nanobubbles on Pt surface, J. Colloid Interface Sci. 582 (2021) 167–176, http://dx.doi.org/10.1016/j.jcis.2020.07.135.

[24] Duncan Dockar, Livio Gibelli, Matthew K. Borg, Shock-induced collapse of surface nanobubbles, Soft Matter 17 (2021) 6884–6898, http://dx.doi.org/10.1039/D1SM00498K.

[25] Hiroshi Tomita, et al., Direct observation of single bubble cavitation damage for MHz cleaning, Solid State Phenom. 145–146 (2009) 3–6, http://dx.doi.org/10.4028/www.scientific.net/SSP.145-146.3,

[26] Valentina Belova, et al., A new approach to nucleation of cavitation bubbles at chemically modified surfaces, Phys. Chem. Chem. Phys. 13 (17) (2011) 8015–8023, http://dx.doi.org/10.1039/c1cp20218a.

[27] Axi Holmström, et al., Gold removal from e-waste using high-intensity focused ultrasound, Ultrason. Sonochemistry 111 (2024) 107109, http://dx.doi.org/10.1016/j.ultsonch.2024.107109.

[28] Eetu Lampsijarvi, et al., Calibrated quantitative stroboscopic schlieren imaging of ultrasound in air, in: 2019 IEEE International Ultrasonics Symposium, IUS, IEEE, United States, ISBN: 978-1-7281-4597-6, 2019, pp. 1651–1654, http://dx.doi.org/10.1109/ULTSYM.2019.8925916, IEEE International Ultrasonics Symposium, IUS ; Conference date: 06-10-2019 Through 09-10-2019.

[29] Nobuhito Ishigure, Osamu . Matsuoka, Bulk-etch rate of CR-39 detector under various conditions of temperature and concentration of NaOH solution, Hoken Butsuri 18 (1) (1983) 17–21.

[30] Johannes Schindelin, et al., Fiji: An open-source platform for biological-image analysis, Nature Methods 9 (7) (2012) 676–682, http://dx.doi.org/10.1038/nmeth.2019.

[31] Arne Vancleed, Imagej-particle-detection-and-analysis, 2020, URL: https://github.com/ArneVancleef/ImageJ-Particle-detection-and-analysis. (visited on 04/18/2025).

[32] Jinjong Kim, et al., Renaissance of chlorine evolution reaction: Emerging theory and catalytic materials, Angew. Chem. Int. Ed. 64 (1) (2025) e202417293, http://dx.doi.org/10.1002/anie.202417293.

[33] STUK - Radiation and Nuclear Safety Authority, Radon in Finland, 2024, URL: https://stuk.fi/en/radon-in-finland. (Accessed 11 November 2024).

[34] David Njus, et al., Ascorbic acid: The chemistry underlying its antioxidant properties, Free Radic. Biol. Med. 159 (May) (2020) 37–43, http://dx.doi.org/10.1016/j.freeradbiomed.2020.07.013.

[35] Shi Wei Gong, et al., Scaling law for bubbles induced by different external sources: Theoretical and experimental study, Phys. Rev. E 81 (2010) http://dx.doi.org/10.1103/PhysRevE.81.056317.

[36] Chunlong Ma, et al., Experimental research on the electric spark bubble load characteristics under the oblique 45 degree curved surface boundary, J. Mar. Sci. Eng. 9 (2020) 32, http://dx.doi.org/10.3390/jmse9010032.

[37] Putong Wang, et al., Detection of limited-energy α particles using CR-39 in laser-induced $p^{-11}B$ reaction, Front. Phys. 11 (2023) http://dx.doi.org/10.3389/fphy.2023.1166347.

[38] Entesar H. EL-Araby, Doaa H. Shabaan, Measurement of alpha particle range in CR-39 detector using nuclear track profiles, J. Radiat. Res. Appl. Sci. 15 (1) (2022) 139–144, http://dx.doi.org/10.1016/j.jrras.2022.01.018.

[39] Edward Morse, Nuclear Fusion, Springer International Publishing, ISBN: 9783319981710, 2018, http://dx.doi.org/10.1007/978-3-319-98171-0.

[40] Stanislaw Szpak, et al., Evidence of nuclear reactions in the Pd lattice, Naturwissenschaften 92 (8) (2005) 394–397, http://dx.doi.org/10.1007/s00114-005-0008-7.

[41] J. Dash, A. Ambadkar, Co-depositon of palladium with hydrogen isotopes, in: Condensed Matter Nuclear Science, World Scientific, 2006, pp. 477–484, http://dx.doi.org/10.1142/9789812774354_0038.

[42] Tadahiko Mizuno, Tadayoshi Ohmori, Michio Enyo, Isotopic changes of the reaction products induced by cathodic electrolysis in Pd, J. New Energy 1 (1996).

[43] Gaurav Yadav, Neelkanth Nirmalkar, Claus-Dieter Ohl, Electrochemically reactive colloidal nanobubbles by water splitting, J. Colloid Interface Sci. 663 (2024) 518–531, http://dx.doi.org/10.1016/j.jcis.2024.02.148.

[44] Sunghak Park, et al., Combined effects of electrode morphology and electrolyte composition on single H2 gas bubble detachment during hydrogen evolution reaction, Nanoscale 17 (2025) 10020–10034, http://dx.doi.org/10.1039/D5NR00234F.

[45] Xuegeng Yang, et al., Dynamics of single hydrogen bubbles at a platinum microelectrode, Langmuir 31 (29) (2015) 8184–8193, http://dx.doi.org/10.1021/acs.langmuir.5b01825, PMID: 26133052.

[46] Çayan Demirkır, et al., Life beyond fritz: On the detachment of electrolytic bubbles, Langmuir 40 (39) (2024) 20474–20484, http://dx.doi.org/10.1021/acs.langmuir.4c01963, PMID: 39305203.

[47] Rui Hao, et al., Imaging nanobubble nucleation and hydrogen spillover during electrocatalytic water splitting, Proc. Natl. Acad. Sci. 115 (23) (2018) 5878–5883, http://dx.doi.org/10.1073/pnas.1800945115.

[48] Shasha Guo, et al., Separating nanobubble nucleation for transfer-resistance-free electrocatalysis, Nat. Commun. 16 (1) (2025) 919, http://dx.doi.org/10.1038/s41467-024-55750-5.

[49] Xiaotian Wang, et al., Ultrasonic assisted electrolysis enables massive production of hydrogen bulk nanobubbles, J. Colloid Interface Sci. 695 (April) (2025) 137748, http://dx.doi.org/10.1016/j.jcis.2025.137748.

[50] Van-Tu Nguyen, et al., Modeling of the bubble collapse with water jets and pressure loads using a geometrical volume of fluid based simulation method, Int. J. Multiph. Flow 152 (2022) 104103, http://dx.doi.org/10.1016/j.ijmultiphaseflow.2022.104103.

[51] Joachim Dzubiella, Interface dynamics of microscopic cavities in water, J. Chem. Phys. 126 (19) (2007) 194504, http://dx.doi.org/10.1063/1.2734962.

[52] Julien Lombard, Thierry Biben, Samy Merabia, Kinetics of nanobubble generation around overheated nanoparticles, Phys. Rev. Lett. 112 (2014) 105701, http://dx.doi.org/10.1103/PhysRevLett.112.105701.

[53] Ding Ma, et al., Characterization of the dynamic behavior of multinanobubble system under shock wave influence, Langmuir 40 (17) (2024) 9068–9081, http://dx.doi.org/10.1021/acs.langmuir.4c00449, PMID: 38628152.

[54] E.A. Brujan, et al., The final stage of the collapse of a cloud of bubbles close to a rigid boundary, Ultrason. Sonochemistry 18 (1) (2011) 59–64, http://dx.doi.org/10.1016/j.ultsonch.2010.07.004.

[55] Adarsh Shekhar, et al., Nanobubble collapse on a silica surface in water: Billion-atom reactive molecular dynamics simulations, Phys. Rev. Lett. 111 (2013) 184503, http://dx.doi.org/10.1103/PhysRevLett.111.184503.

[56] Vitaly B. Svetovoy, et al., Combustion of hydrogen-oxygen mixture in electrochemically generated nanobubbles, Phys. Rev. E 84 (2011) 035302, http://dx.doi.org/10.1103/PhysRevE.84.035302.

[57] Alexander Prokaznikov, Niels Tas, Vitaly Svetovoy, Surface assisted combustion of hydrogen-oxygen mixture in nanobubbles produced by electrolysis, Energies 10 (2) (2017) http://dx.doi.org/10.3390/en10020178.

[58] Tetsuo Sakai, Hiroyasu Takenaka, Eiichi Torikai, Gas diffusion in the dried and hydrated nafions, J. Electrochem. Soc. 133 (1) (1986) 88–92, http://dx.doi.org/10.1149/1.2108551.

[59] Professional Plastics, CR-39 homalite sheet, 2025, URL: https://www.professionalplastics.com/CR39-HOMALITESHEET. (Accessed 12 June 2025).

[60] Alicja Krystyna Krella, Degradation and protection of materials from cavitation erosion: A review, Materials 16 (5) (2023) http://dx.doi.org/10.3390/ma16052058.

[61] G.V. Samsonov, Mechanical properties of the elements, in: G.V. Samsonov (Ed.), Handbook of the Physicochemical Properties of the Elements, Springer US, Boston, MA, ISBN: 978-1-4684-6066-7, 1968, pp. 387–446, http://dx.doi.org/10.1007/978-1-4684-6066-7_7.

[62] Haider K. Ali, Toughening Polymer Surfaces (Ph.D. thesis), University of Wollongong, Australia, 2009, URL: https://ro.uow.edu.au/articles/thesis/Toughening_polymer_surfaces/27828960.

[63] Lev I. Krishtalik, Kinetic isotope effect in the hydrogen evolution reaction, Electrochim. Acta 46 (19) (2001) 2949–2960, http://dx.doi.org/10.1016/S0013-4686(01)00526-6.

[64] Sunghak Park, et al., Solutal marangoni effect determines bubble dynamics during electrocatalytic hydrogen evolution, Nat. Chem. 15 (11) (2023) 1532–1540, http://dx.doi.org/10.1038/s41557-023-01294-y.

[65] Ines M. Hauner, et al., The dynamic surface tension of water, J. Phys. Chem. Lett. 8 (7) (2017) 1599–1603, http://dx.doi.org/10.1021/acs.jpclett.7b00267, PMID: 28301160.

[66] J.R. Heiks, et al., The density, surface tension and viscosity of deuterium oxide at elevated temperatures, J. Phys. Chem. 58 (6) (1954) 488–491, http://dx.doi.org/10.1021/j150516a010.

[67] T.W. Jeong, et al., CR-39 track detector for multi-MeV ion spectroscopy, Sci. Rep. 7 (1) (2017) http://dx.doi.org/10.1038/s41598-017-02331-w.

[68] Matiullah, et al., Discovery of new etchants for CR-39 detector, Radiat. Meas. 39 (3) (2005) 337–343, http://dx.doi.org/10.1016/j.radmeas.2004.06.012.

[69] Takao Tsuruta, Takeo Niwa, Yoshimi Fukumoto, Experimental study of CR-39 etched track detector for fast neutron dosimetry, J. Nucl. Sci. Technol. 29 (11) (1992) 1108–1115, http://dx.doi.org/10.1080/18811248.1992.9731642.

[70] C.S. Oliveira, et al., Low energy alpha particle tracks in CR-39 nuclear track detectors: Chemical etching studies, Nucl. Instrum. Methods Phys. Res. Sect. A: Accel. Spectrometers Detect. Assoc. Equip. 995 (2021) 165130, http://dx.doi.org/10.1016/j.nima.2021.165130.

[71] Yang-Fan He, et al., Calibration of CR-39 solid-state track detectors for study of laser-driven nuclear reactions, Nucl. Sci. Tech. 31 (4) (2020) http://dx.doi.org/10.1007/s41365-020-0749-1.

[72] E.M. Awad, Direct determination of track etch rate and response of CR-39 to normal incidence high-energy heavy ions, Radiat. Meas. 33 (6) (2001) 855–858, http://dx.doi.org/10.1016/S1350-4487(01)00098-1.